4U DEPLOYABLE TELESCOPE FOR SMALLSATS

Jeroen De Maeyer[(1)], Maarten Kempenaers[(1)], Dirk Vandepitte[(1)]

[(1)] *KULeuven Department of mechanical engineering, Celestijnenlaan 300, 3001 Heverlee*
jeroen.demaeyer1@kuleuven.be, maarten.kempenaers@kuleuven.be, dirk.vandepitte@kuleuven.be

ABSTRACT

The 4U deployable telescope improves light gathering capabilities and image quality in comparison with current rigid telescopes for CubeSats of the same size. A deployable structure increases the separation between the primary and secondary mirror and a deployable baffle structure attenuates stray light. The deployment mechanism consists of titanium longerons which in collapsed state deform into a helix and store the energy needed to erect the structure without an extra actuator. As deployable structures are in general less stiff, the structure is more sensitive to vibrational disturbances. A High Precision Pointing Platform (HPPP) controls the light inside the optical path without affecting the spacecrafts attitude. This system is designed to counteract small structural deformations and pointing jitter which the spacecraft's Attitude Determination and Control System (ADCS) cannot compensate. Therefore, the HPPP platform uses a dedicated measurement system and fine steering mirror (FSM) which operate in a feedback control loop. This paper summarizes the current status of the ongoing project.

1 INTRODUCTION

High quality space or earth observation data are usually acquired from large multi-million euro space platforms with long revisit times, making the data expensive. Despite the large cost, the demand for high quality data increases in both earth and space observation applications. A large range of new products and services would become feasible if the cost of data would decrease, or if the quality of data would increase. The availability of the same data from a smaller platform like CubeSats with lower development and launch costs reduces the cost.

As image quality improves with telescope size, larger optics give a clear advantage. The mirror size and focal length are usually limited by the spacecraft dimensions and size of supporting equipment onboard the spacecraft. Realizing that dimensional limits of the spacecraft mainly apply during launch opens the possibility to combine the strength of small spacecraft with the advantages of large optics through deployable structures. During launch the optics are folded such that they fit within a small volume but once separated from the launch vehicle the structure deploys to its final size. Main design challenges of deployable structures are the stricter dimensional limits, the more difficult attitude control and a higher sensitivity to disturbances. As deployable structures generally are less stiff in comparison to their rigid counterparts, they are more sensitive to structural deformations caused by vibrations. Structural deformations and pointing inaccuracies that the Attitude Determination and Control System (ADCS) cannot control can be compensated through a High Precision Pointing Platform (HPPP). The HPPP controls the data acquisition payload on top of the ADCS, in case of a telescope this platform works in parallel with the ADCS and steers the light in the optical path without affecting the spacecraft attitude.
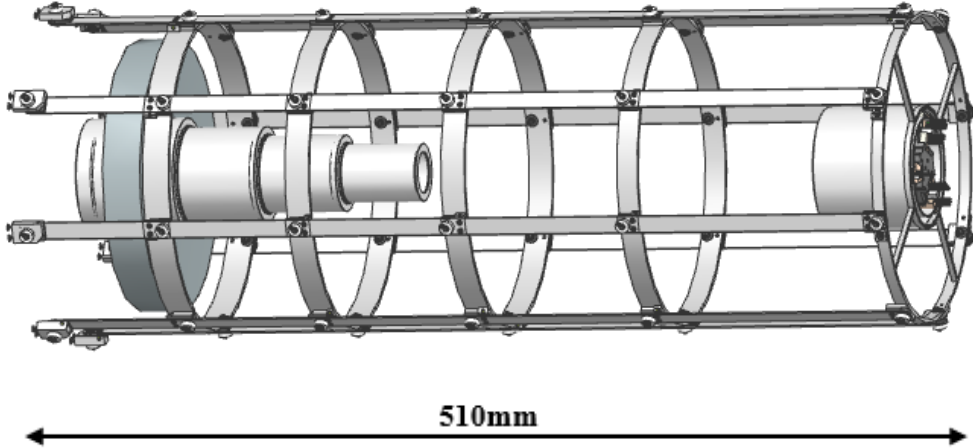
510mm

Figure 1: 3D sketch of the telescope in deployed state with removed baffle around M1 for clarity.

The goal of the development is a deployable Cassegrain telescope that fits within four units of a CubeSat in stowed condition. The design concept should be scalable to different satellite sizes and shapes. As reference case, the project uses a 1600mm focal length Cassegrain telescope, shown on figure 1. The telescope has a field of view of +/-0.15°, a primary mirror (M1) diameter of 180mm and a primary- secondary mirror (M2) separation of 450mm. Table1 gives the alignment tolerances for this telescope, the used diffraction limit is the root mean square departure of the wavefront which may not exceed λ /14 [11, 22]. This design corresponds with a ground sampling distance (GSD) of 1.7m at 500km altitude in case the diffraction limit is reached.

		Aberrations (static)		Spot displacement (dynamic)	
		Min	Max	Min	Max
Axial shift	$[\mu m]$	-7.25	7.25		
Tilt M2	[°]	-0.12	0.12	0.00008	0.000113
Lateral shift M2	$[\mu m]$	-344	344	0.9	1.27
Lateral shift with tilt compensation	$[\mu m]$	-900	900	300	424.26

Table 1: Tolerances for the reference case.

2 DEPLOYMENT STRUCTURE

Many space mission have deployable structures onboard, the best known examples are solar arrays and antennas. However, the required accuracy of those structures is relatively mild in comparison to the requirements for optical instruments. Deployable structures with an optical payload which have stricter tolerances are becoming much more widespread. This new trend is in the first place applicable to larger platforms, this paper presents a feasibility study of deployment mechanisms on smaller platforms. Some examples of larger platforms with deployable optics are the James Webb Space Telescope [15] and IXO, the International X-ray Observatory [27]. These missions have an active onboard system to deploy an articulated boom together with part of the optical system. Conceptual studies on smaller platforms have been carried out by NASA [4] for a 6U CubeSat, and by TUBerlin [24] for a SmallSat (100 kg). Surrey Satellite Technologies Limited (SSTL) proposes a telescopic barrel deployment of the secondary mirror [7] and UKATC's prototype demonstrates a deployable telescope packaged within a 1.5U CubeSat volume [23]. The University of Tokyo launched the PRISM satellite with a successful deployment [16]. However, due to the low stiffness of the deployable structure and

the low pointing stability of the platform, the GSD was no better than 30m. The unavailability of stable SmallSat pointing systems has long hindered the use of deployable telescopes. Recent advances in this area have demonstrated the feasibility of high-precision pointing for optical instruments on small spacecraft [2, 17].

The main structure of the 4U deployable telescope consists of a coilable boom which relies on elastic energy for deployment. The elastic element consists of eight titanium longerons and five supporting rings which articulate via self-locking hinges. In collapsed state the longerons deform into a helix and store the elastic energy to erect the structure. Deployment motion is a combination of a translation and a rotation, in folded configuration the top ring rotates over 304° with respect to the deployed state. Figure 2 shows the deployment sequence on the prototype which is developed at KU Leuven [10].
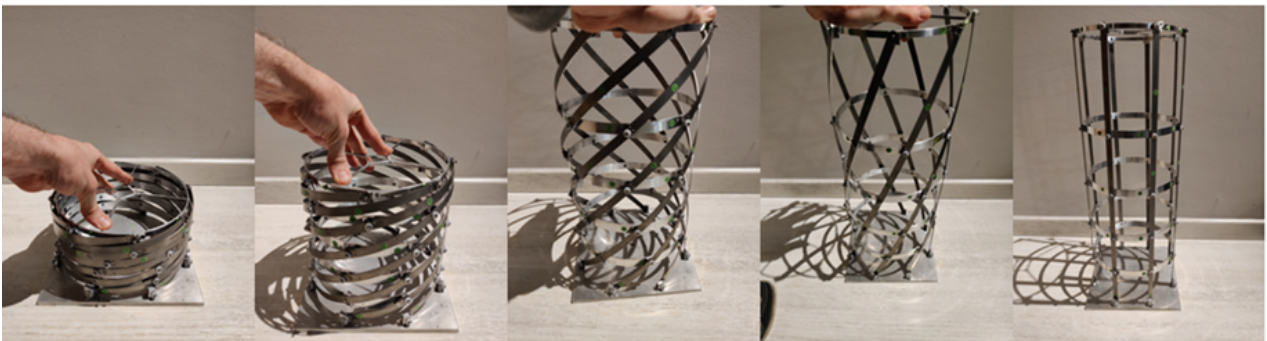

Figure 2: Deployment sequence of the structure [10].

2.1 Structural design

Material selection of the different components is the first step in the design process. The main objectives are to minimize the mass and cost of the components. Initially the free variable and the specific primary and secondary needs are determined for each component. The material indices are derived from the primary needs and implemented in the material selection software, CES Edupack 2018 [5]. The final material is selected from the previous determined list, based on the machinability and availability. Table 2 lists an overview of the materials used in the prototype [10].

Part	Materials
Beams	Titanium, alpha-beta alloy, Ti-6Al-4V, aged
Rings	Aluminum, 2024, T8510/8511
Axis	Stainless steel EN 1.4125
Hinges	Steel C45

Table 2: Overview of the materials used in the prototype [10].

The distance between the primary and secondary mirror is 450mm, additionally there is space needed for the rest the optical system. Therefore, the length of the longerons is increased to 510mm. The longerons need to be as thick as possible to obtain a stiff structure in deployed state. Contradictory, during the collapsing sequence the mechanical stresses in the longerons increase with the longeron thickness. A compromise is made and the longeron thickness is set to 1mm such that the longerons stay in the elastic regime [10].
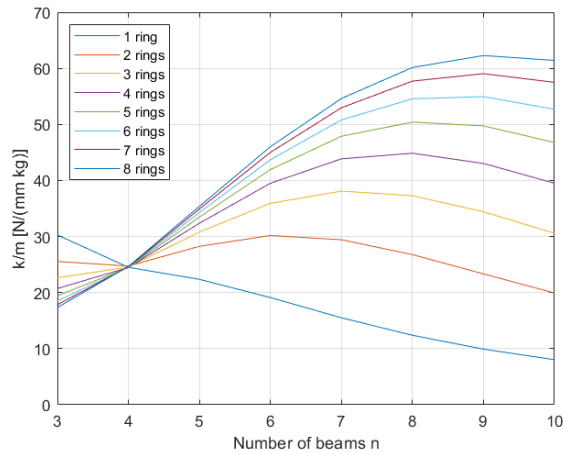
Figure 3: Ratio stiffness over mass for all combinations of longerons and rings [10].

The optimal number of longerons and rings is determined by minimizing the mass of the structure and maximizing the stiffness to ensure a good alignment of the optical system in deployed state. Hence, the ratio bending stiffness over mass is used to compare the different configurations. Figure 3 summarizes the results for any number of longerons and rings. The optimal combinations are further optimized with the objective to maximize the first eigenfrequency and to minimize the mass. The cross sectional dimensions and the position of the rings are chosen as the optimization variables. There is no single optimum as these two objectives are contradictory. Figure 4a shows the pareto front, these points represent an optimum with a different compromise between mass and first eigenfrequency. A different optimal point will improve one objective while sacrificing the other. The blue point is the selected design point, the red points are not possible because at those point two rings collide in stowed condition. Figure 4b gives an illustration of the rings of the final design in stowed configuration [10].
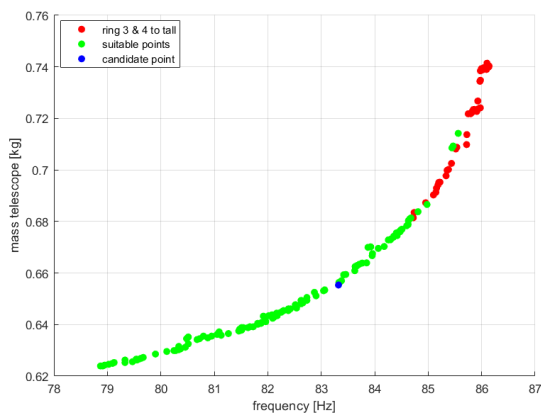
(a) Pareto front
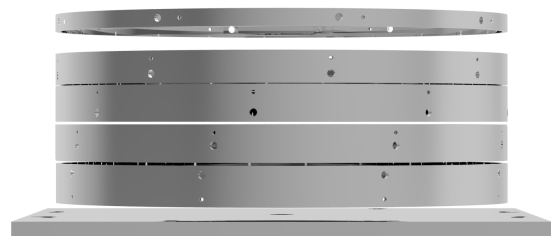
(b) Rings in stowed configuration

Figure 4: Results of the optimization for the structure with 8 longerons and 5 rings [10].

Finite element analyses are used to simulate the deployment system during operation. In the first place a non-linear simulation is performed to ensure the longerons do not plastically deform during deployment. Figure 5 shows the obtained FEM results. The maximal Von Mises stress in the titanium longerons is around 900MPa, which is lower than the Yield strength of 1050MPa. Hence, the longerons remain in the elastic regime [10].

(a) Deformation

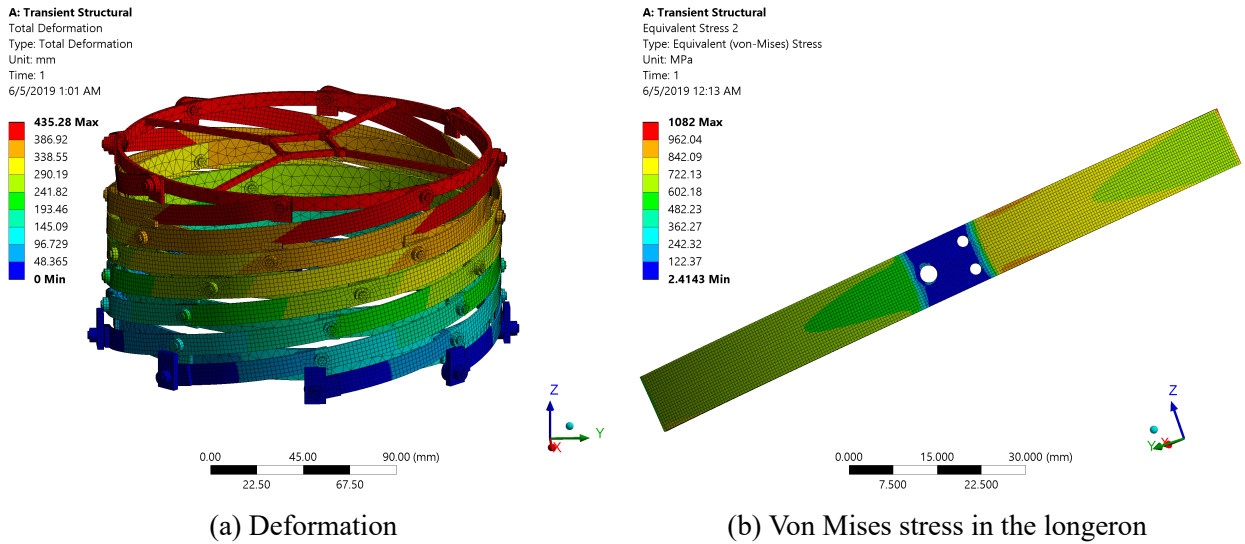(b) Von Mises stress in the longeron

Figure 5: FEM analysis of the deployable structure during deployment [10].

A modal analysis, performed on the entire 6U CubeSat, examines the dynamic behavior of the system. Figure 6 illustrates the mode shapes and table 3 lists the description of the modes and their corresponding eigenfrequencies up to 160Hz, the operating frequency range of the reaction wheels [10].

(a) 1st mode

(b) 2nd mode

(c) 3th mode
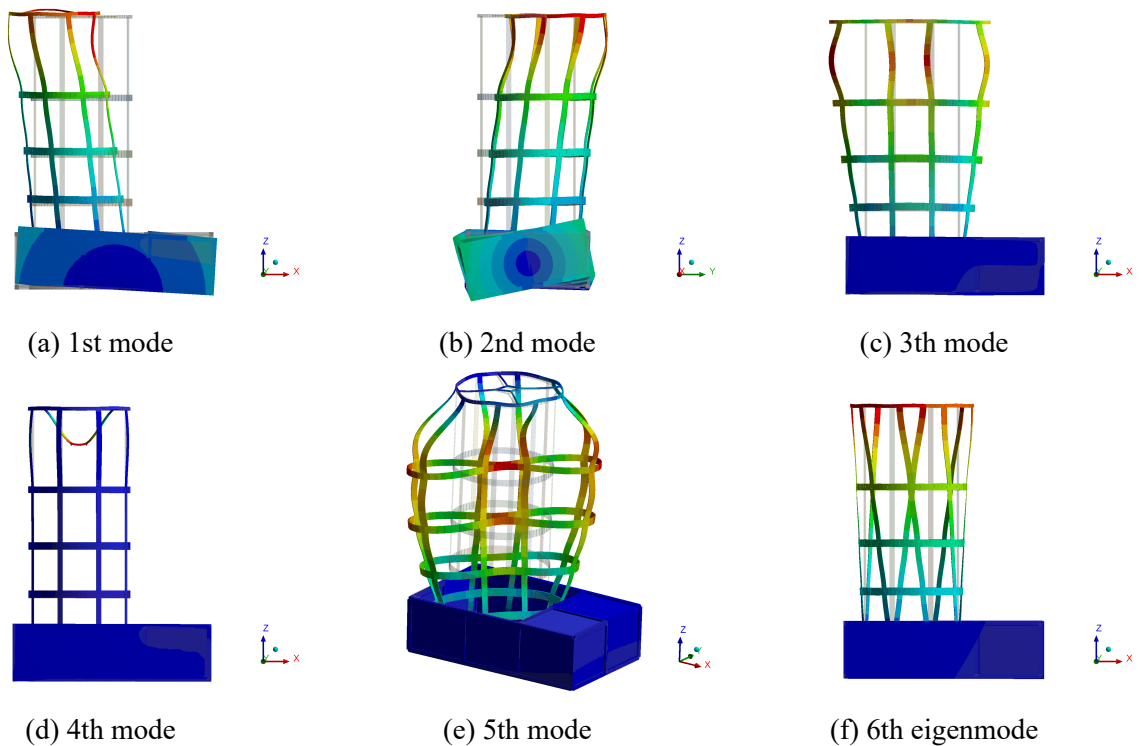
(d) 4th mode

(e) 5th mode

(f) 6th eigenmode

Figure 6: Representation of the first six eigenmodes of the total satellite structure [10].

The initial prototype is successful considering that the longerons do not deform plastically in stowed condition and that the structure deploys independently. However, the energy stowed in the structure is large, leading to a very fast deployment and a large shock at the end of the deployment. This shock may damage the structure or the onboard instruments and should be damped in the next design iteration [10].

Mode	Frequency [Hz]	Description
1	89.3	Bending mode in x-direction
2	90.2	Bending mode in y-direction
3	108.8	Pumping of the top-section
4	118.2	Pumping of the secondary mirror mount
5	126.3	Pumping of the complete beam
6	141.0	Torsional mode around z-axis

Table 3: Eigenfrequencies of the total satellite structure and its description [10].

2.2 Self-locking hinge

During deployment the longerons rotate with respect to the rings. Therefore, the hinges connecting the rings and longerons need one rotation degree of freedom during deployment. In deployed state, the structure needs a high stiffness to ensure a good mirror alignment and a low sensitivity to vibrations. A self-locking hinge is introduced to increase the structural stiffness in deployed state. A wide range of locking mechanism concepts includes a magnetic hinge, a spring preloaded clicking hinge, shape memory alloy, welding the hinge once deployed, glue capsules rupturing during deployment, hinges with actuators, etc. Within this project the magnetic locking hinge and the spring preloaded clicking hinge are compared.

Figure 7 shows the design of the magnetic hinge. A neodymium magnet with a diameter of 2mm and a thickness of 1mm attracts its counteracting part, a ferromagnetic steel C45 part. An end stop blocks the rotation motion at the end of the deployment phase. Magnetostatic simulations estimate a total locking force between the two components of 130mN. At first glance this locking force seems to be sufficient as there are 48 locking hinges, and each of them contributes to the mutual goal to lock the structure. However, after testing the locking force shows to be too small. The magnetic force decreases drastically as the distance between the attracting parts increases. Hence, the locking force is too low to lock the structure. Decreasing the distance between the attracting parts increases the total magnetic force in the next design iterations [10].
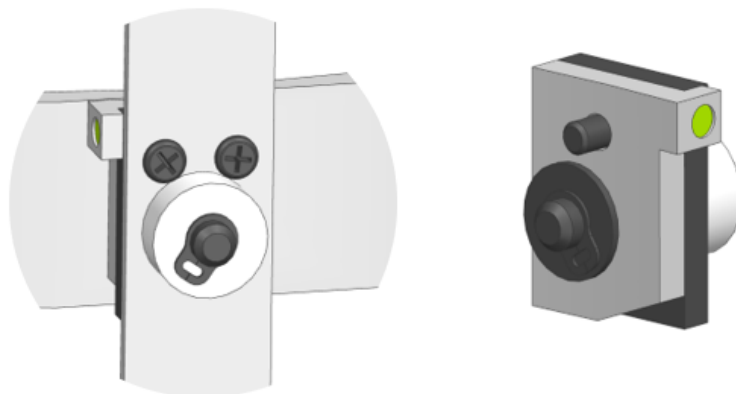

Figure 7: Conceptual illustration of the magnetic locking hinge [10].

The alternative concept uses an elastic clip that clicks into place at the end of the deployment phase. Figure 8 shows the design of the mechanically locking hinge. During deployment the rotating part attached to the longeron slides over the elastic clip. Once fully deployed, the spring clicks into place and constrains the rotational DOF by pushing its counterpart against the end stop. The elastic clip is manufactured from spring steel using wire-EDM and has a minimal thickness of 0.4mm. The per-

formance of the design is computed using FEM analysis. The maximal Von Mises stress is 315MPa, which is lower than the yield strength of 1000MPa. The total contact force in the rotational direction is 3.5N, which is considerably higher than the locking force in the current magnetic locking hinge. This design is tested on the current prototype and two main shortcomings are observed. (1) The elastic clip does not stay in place once deployed but can easily be moved out of the way by the longeron, this is due to the immature design of the tip of the clip. (2) The hinge should not only limit the rotation motion of the longerons but should press the longerons against the ring such that there is no play between these parts [26].
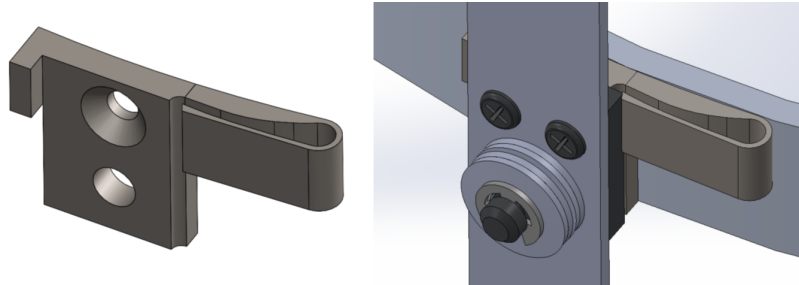

Figure 8: Conceptual illustration of the mechanically locking hinge [26].

3   STRAY LIGHT DESIGN

Stray light is unwanted light that reaches the focal plane of an optical system. Baffles are introduced into the telescope to overcome this issue. These baffles block the low-order stray light paths and are the primary means of controlling stray light in the optical system. In its most simple form, a baffle consists of a cylindrical or conical tube which encloses the optical system, a high absorbent coating attenuates the reflected light. The baffle performance can further be improved by adding vanes, flat structures attached to the baffle wall, which block scattered light from the baffle wall. The primary objective of the baffle is to block light from outside the field of view (+/-0.15°) and is designed to not vignette. Vignetting occurs when the image forming light bundle is blocked by different structures in different planes along the optical axis and consequently reduces the image brightness towards the periphery [6].

The 4U deployable telescope structure comprises three baffles, the large main baffle out- or inside the deployment structure, one around the centre hole of the primary mirror and the last one around the secondary mirror assembly. The main baffle around the telescope structure prevents direct illumination of the primary mirror. The baffle in the centre of the primary mirror and the one around the secondary mirror block the zero-order external stray light path through the hole in the primary mirror. Figure 9 shows the position and a first impression of these three baffles. Only the baffle around the primary mirror centre hole has vanes because for the other baffles it would increase the complexity considerably while the gain is only minimal. Optimal baffle dimensions are calculated analytically and verified using ray tracing software, Zemax [25]. All baffles deploy together with the telescope structure.
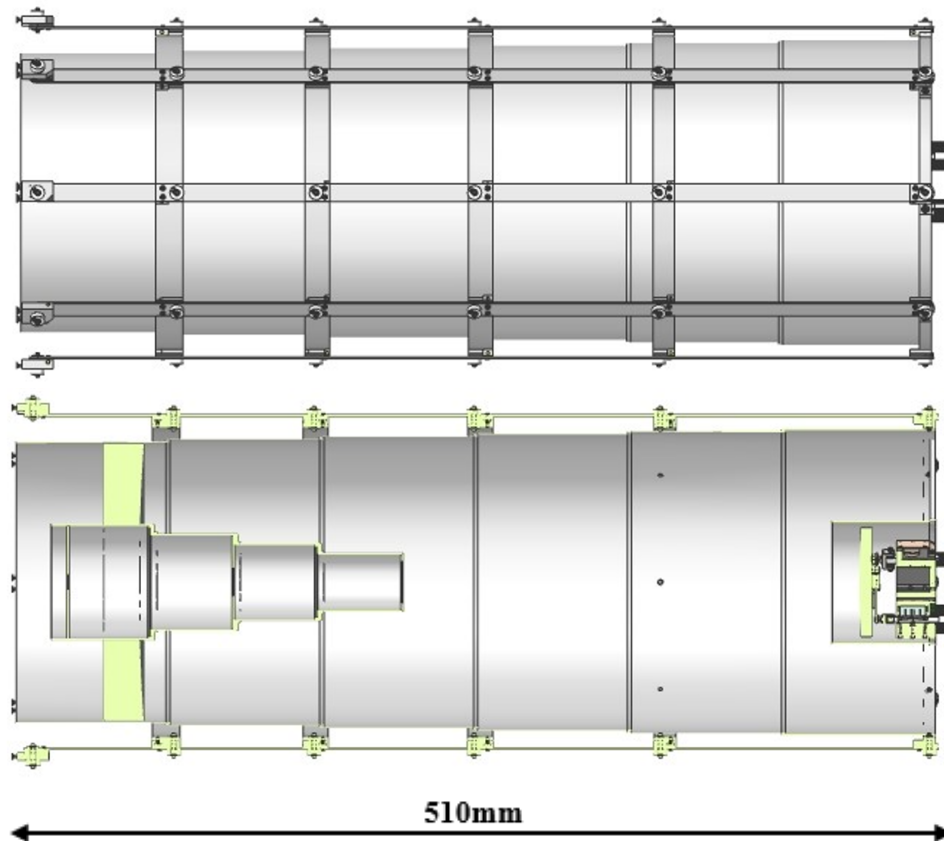
Figure 9: Conceptual sketch of the telescope in deployed state.

4 HPPP-LOOP

A two-stage control strategy brings the telescope performance within desired tolerances [2]. A first stage, the outer loop on figure 10, comprises an ADCS box with the necessary sensors (sun, earth, star tracker, etc.) and controls the spacecraft attitude. A commercially available solution can be used as long as it is capable to control the spacecrafts attitude within working range of the second stage. The inner loop on figure 10 further improves the pointing performance, it consists of a fine steering platform controlling the data acquisition payload without affecting the spacecrafts attitude. The main components of this second stage are one or more fine steering mirrors, a fine measurement system and a controller that closes the feedback loop. The control loop calculates correction signals with the results supplied by the measurement system (MS) and sends them to the fine steering mirror (FSM). By changing the mirror tip/tilt and displacement along the optical axis the optical path is adapted to counteract disturbances.

The inner control loop itself has also two components, a slow control loop which aligns the telescope before measurements and compensates for slow thermal deformations, and a faster control loop to counteract vibrations and pointing jitter. The alignment procedure to bring the telescope within static tolerances can be based on wavefront error estimations made during succeeding steps where in every step the error should decrease [21]. A higher bandwith (30Hz or more) control loop with a dedicated measurement system compensates the higher frequency disturbances and pointing jitter.
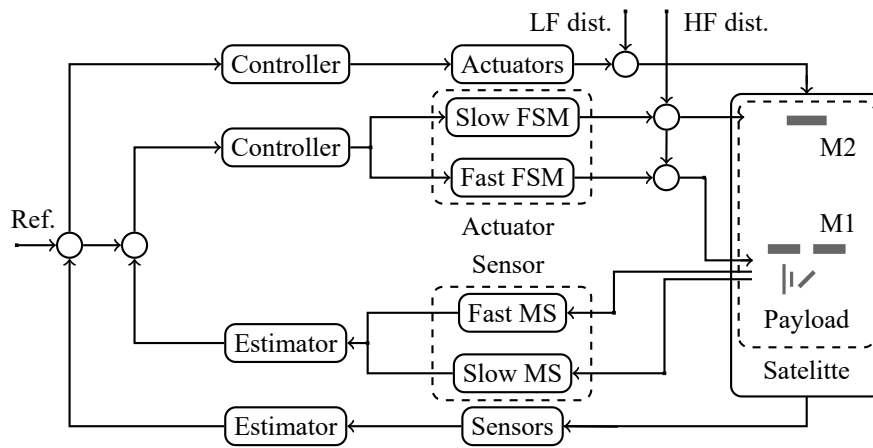
Figure 10: Control strategy for the 4U deployable telescope with the combined control loop of the ADCS (outer loop) and HPPP (inner loop).

4.1 Fine steering mirror

The dimensional limits on Small- and Cubesats impose very strict requirements on the FSM design on top of the already very strict requirements on vacuum compatibility, thermal, control, dynamic behaviour, etc. Commercially available mirrors often combine amplified piezo actuators with relatively large rods (+/-10mm) to connect mirror and actuators, which is a space consuming solution with limited tip/tilt range [1]. To combine all those aspects (large mirror, long stroke, limited volume) a less common design for a movable secondary mirror is investigated. The combination of piezowalkers or steppers and a leaf spring to connect actuators and mirror [1] allows to combine the long stroke of the actuators with the limited volume of the leaf spring. Figure 11 shows some first design concepts of the proposed solution, with 3 Piezomotor LT20 actuators connected to the mirror with a Y-shaped leaf spring. All models share the same leaf spring design but differ in the linear guide attached to leaf spring and actuator.

Table 4 shows some results of static linear analyses of the models shown on figure 11. All linear guides are clamped along their circumference while the other boundary conditions are equal to the strokes as mentioned in the table. All simulations use a 65mm diameter and 8mm thick mirror, the

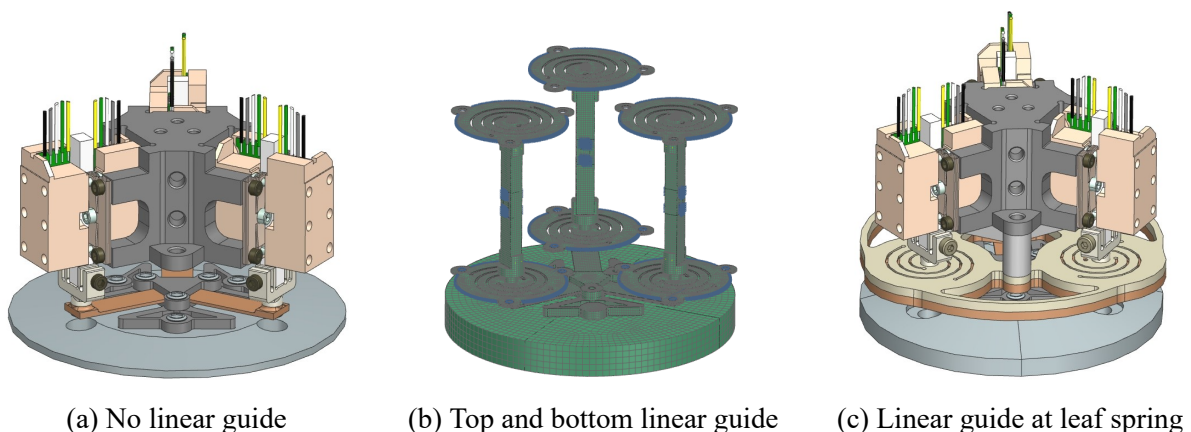| (a) No linear guide | (b) Top and bottom linear guide | (c) Linear guide at leaf spring |

Figure 11: Design of different simulated FSM solutions, all designs combine Piezomotor LT20 actuators with a leaf spring. Figures (a) and (c) show a first design for the test set-up while (b) shows a FEM model. CAD models of Piezomotor LT20 from [19].

aluminum leaf spring has a thickness of 0.6mm. The aluminum linear guides are all constructed from 0.4mm thick sheet material. The rotations are measured along two perpendicular axes in the mirror plane with one axis pointing towards one of the connection points between leaf spring and actuator. The simulations show large tip tilt angles above 1.3° and the stroke along the optical axis is only limited by the length of the actuator rods. All designs have a small coupled rotation, so a rotation around one axis results only in a very small rotation around the other perpendicular axis.

Simulation		1a	1b	1c	2a	2b	2c	3a	3b	3c
Act 1 stroke	[mm]		0.4			0.4			0	
Act 2 stroke	[mm]		-0.5			-0.2			-0.35	
Act 3 stroke	[mm]		0.1			-0.2			0.35	
Rotation axis 1	[°]	1.35	1.34	1.33	1.35	1.34	1.33	9E-05	1E-03	2E-04
Rotation axis 2	[°]	1.17	1.16	1.15	3E-05	3E-05	2E-04	1.37	1.35	1.35
Displacement in mirror plane	[mm]	0.33	0.33	0.33	0.25	0.25	0.25	0.25	0.25	0.25
Displacement along optical axis	[mm]	8E-05	4E-05	8E-06	6E-05	5E-05	2E-04	2E-05	1E-04	2E-04
Force act 1	[N]	0.32	0.82	1.42	1.28	1.65	2.80	2.24	2.89	4.91
Force act 2	[N]	3.52	4.11	7.03	1.28	1.66	2.80	2.24	2.89	4.92
Force act 3	[N]	3.20	3.31	5.61	2.56	3.30	5.62	8E-06	2E-04	8E-03

Table 4: Results for linear static analyses of the models shown on figure 11, the letters mentioned on the simulation line correspond to the specific model on the figure. Rotations, translations and forces are absolute values.

Figure 12 visualizes the Von Mises elemental stress distribution in the leaf spring during simulation 1a of table 4 and the first bending mode. The maximal stress value lies well below the yield strength of high strength aluminum alloys. The first eigenfrequency, 88Hz, of the model described by figure 11a is rather low and lower than the one required by most launch providers. The mode corresponds to a mode of the leaf spring, consequently the linear guides have a limited influence on the frequency. After design modifications the lower eigenfrequencies increase by thickening the leaf spring, changing its material or decreasing the moving mass of a thinner mirror. The LT20 actuator has a recommended operating range of 0-10N [20], so all static forces are achievable. Changing the leaf spring properties also changes the required actuator force but some margin is left for most designs. The simulations show the largest tip/tilt angles and the smallest axial actuator forces for the design on figure 11a, which is also the least complex design. Tests will verify the different simulation results.

Separation of design requirements simplifies the design complexity and is indicated on figure 10. This solution uses two FSMs, one containing the M2 mirror, with high tip/tilt angles and a lower bandwidth and one with lower tip/tilt angles but higher bandwidth. The low bandwidth FSM is then used by the slower control loop which compensates for thermal deviations and is used during alignment, while the faster control loop uses the high bandwidth mirror, with higher eigenfrequencies. The high bandwidth mirror is in this case positioned just before the image sensor in the optical path. The setup separates the requirements of large angles and high bandwidth, which are otherwise harsh to combine. Another advantage is the lower needed mirror resolution in comparison with the one FSM lay-out. The lower distance between mirror and sensor decreases the amplification of small tip/tilt errors.

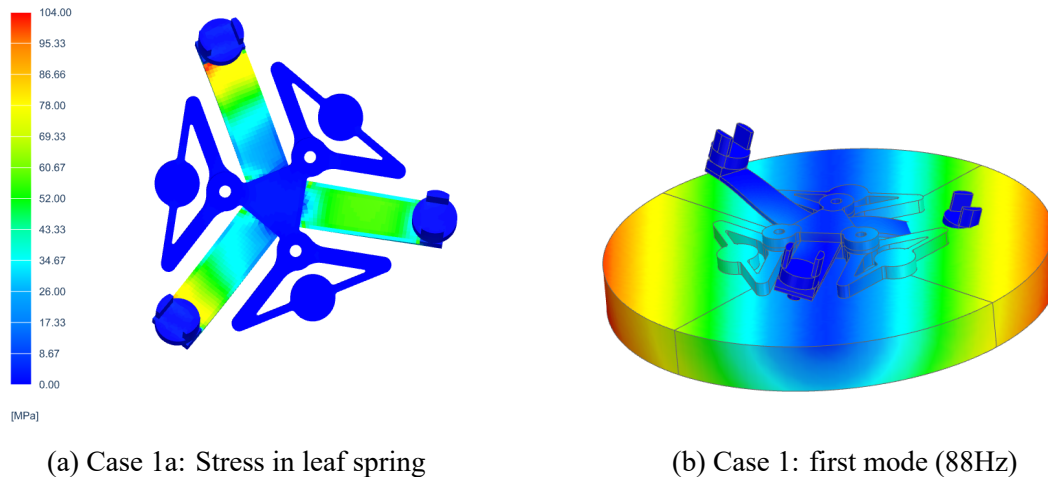(a) Case 1a: Stress in leaf spring   (b) Case 1: first mode (88Hz)

Figure 12: Finite element results for the design of figure 11a, figure (a) indicates the Von Mises stress distribution for simulation 1a in table 4 and figure (b) shows the first eigenmode (88Hz).

4.2   Measurement system

The system should be capable of measuring two type of errors, structural deformations and pointing jitter. In theory an image sensor combined with the appropriate algorithm can measure both type of errors. However for structural deformations, which lead to a measurable misalignment of the telescope, this results in too long measuring and calculation times as larger images and in consequence longer processing times are needed. Moreover not every image is suited for misalignment estimations, so performance depends on the scene on the picture. Correlation of two images taken with the image sensor close after each other allows to estimate the pointing jitter. This method calculates the pointing jitter from of the x- and y-shift between the two successive images. To get the required accuracy (table 1) subpixel correlation algorithms are needed as most sensors have pixel sizes of a few μm.

Figure 13 compares the most used 2D-correlation algorithms, the FFT and spatial based algorithms have pixel accuracy and the implementation is based on their mathematical definition. The subpixel FFT algorithm, with subpixel accuracy, is implemented as described by Guizar-Sicairos et al. [9]. The Reduced (Red.) algorithms use spatial techniques but for a reduced search field decreasing the calculation time. In this particular case an 11x11 search field with the zero shift value in the middle is used. Performance and accuracy are measured using Python 3.8 on a HP Elitebook 840 G6 with Intel Core i7-8665U processor and 32GB RAM. The figure clearly indicates that the calculation time (point or lines) and accuracy (bars) increase with image size and that the normalized implementations have in general a better performance in comparison to the unnormalized ones. More detailed images result in a higher accuracy when calculating x- and y-shifts and allow much smaller image sizes and calculation times. The reduced algorithms, in combination with a gradient based method for subpixel accuracy, show promising results with quite constant performance for all image sizes and limited calculation times. However it is only applicable in combination with an accurate ADCS system that brings the pointing jitter within working range of the HPPP and create pixel shifts lower than the search window.
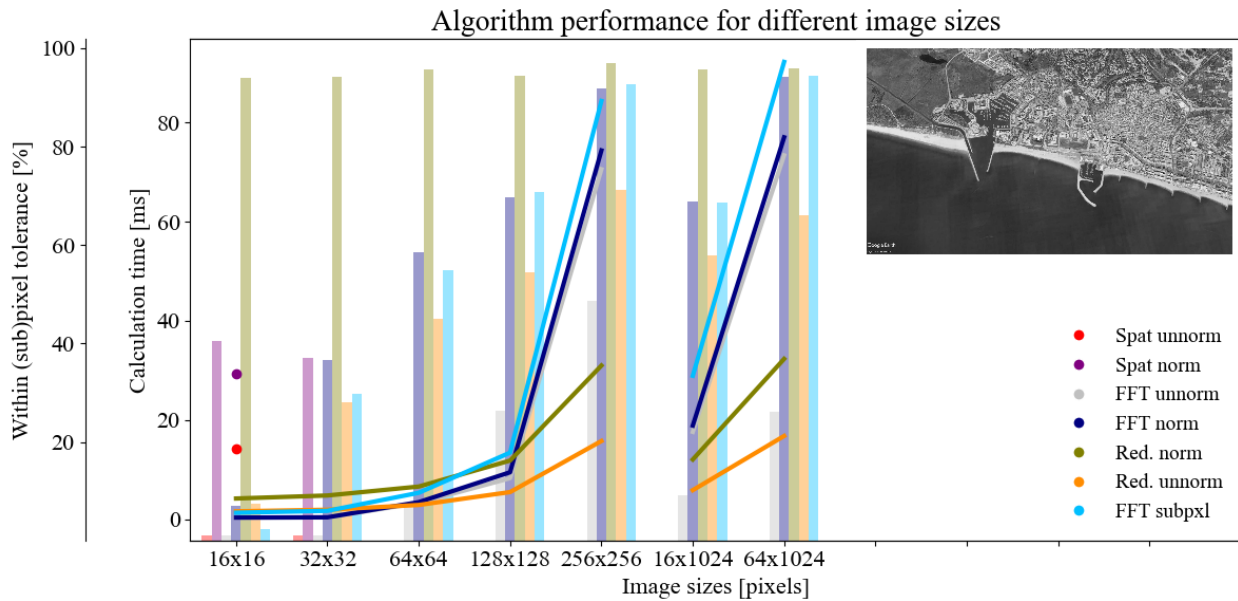
Figure 13: Performance overview for different correlation algorithms and image sizes. All images were part of the image shown on the figure, the tolerance level was set to one pixel except for the subpixel FFT which had a tolerance of 0.1 pixel. Every point on the graph shows the mean value of 1000 simulations. Image data from Google Earth and Terrametrics [8]

Lasers and star trackers provide attractive opportunities to measure structural deformations and multiple examples in literature can be found. The Nustar X-ray Observatory uses a laser and position sensitive device (PSD) to estimate the deformation of a 10m long deployable boom. The system measures the cross-boresight translations and the clocking movement, the rotation around the axis through laser and sensor, at a rate of 100Hz [18, 13, 14]. The Shuttle Radar Topography mission used an adapted startracker camera and fiducials, bright light spots, attached to the structure to estimate the deformation of a 60m long beam. Measurements along 6 degrees of freedom are done at a rate below 10 Hz [3]. A similar system, with more fiducials, was proposed by Liebe et al. [12]. The 4U deployable telescope project investigates solutions which use low power lasers pointing towards the M1 or M2 mirror, or attached to M2. Afterwards, they are reflected through the rest of the optical path until they are captured by an image sensor. Figure 14 shows a conceptual sketch of one of such system with one of three laser arms (in red) of the system shown. The system should be capable to compensate for rotations between the optical axis of the M1 and M2 mirror and to measure translations perpendicular to the optical axis of the telescope at a frequency of at least 30Hz. Changes in axial separation distance between M1 and M2 caused by vibrations are expected to be small such that they are only of importance during initial alignment and for thermal compensation [10]. As thermal deviations are of much lower frequency the bandwidth requirements of this measurement system are less strict.
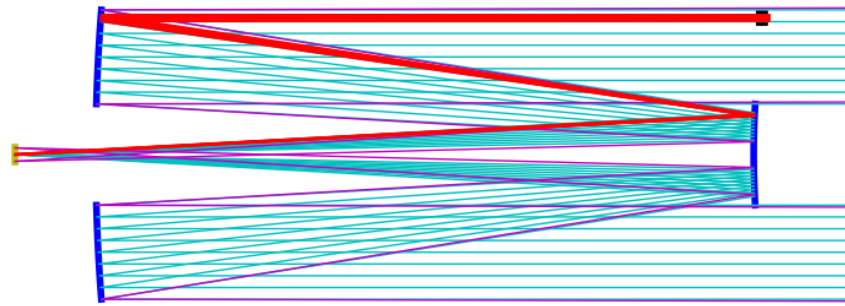
Figure 14: Conceptual idea behind one possible measurement system design (side view), the laser arm is indicated in red. The figure also shows some telescope rays within the field of view.

5 CONCLUSIONS

This paper presents the initial concept of a 4U deployable telescope. The use of deployable structures increases the primary mirror surface and mirror separation distances. A 1600mm focal length Cassegrain telescope with a M1-M2 mirror separation of 450mm is used as design case. The telescope structure consists of a deployable boom structure based on longerons in elastic deformation. A first prototype has eight longerons and five structural rings with good results. Much energy is stored in the system when fully folded which results in a large shock at the end of the deployment phase which should be damped. The baffle structure that deploys with the structure contains three baffles, a large one around the primary mirror, a second one around the secondary mirror and a last one in the center hole of the primary mirror. An HPPP control loop attenuates and compensates for jitter and small deformations which are inherent to small spacecraft and deployable structures. A dedicated measurement system measures both type of errors whereafter corrective signals are send to one or more fine steering mirrors. First analyses of a less common FSM design, show promising results with large tip/tilt ranges and axial translations. The design combines the long stroke of piezozwalkers with the limited volume of a leaf spring.

6 REFERENCES

[1] De Maeyer J., *Ontwerp van een precies piëzo-aandrijfmechanisme voor de spiegel van een CubeSat in een astronomiemissie* [Master's Thesis, KULeuven], 2020, Limo. .

[2] De Munter W., Delabie T. and Vandepitte D., *Development of a high-precision pointing platform for small spacecraft*, 4S Sympoosium, 2018.

[3] Duren R. M. and Liebe, C. C., *The SRTM sub-arcsecond metrology camera*, IEEE Aerospace Conference Proceedings (Cat. No.01TH8542), pp. 4/2037-4/2046 vol.4, doi: 10.1109/AERO.2001.931535.2001, 2001.

[4] Elwood A. F., Ennico-Smith K. and Rademacher A. T., *Collapsible Space Telescope (CST) for Nanosatellite Imaging and Observation*, 27th Annual AIAA/USU Conference on Small Satellites.

[5] Fayazbakhsh K. and Abedian A., *Materials selection for applications in space environment considering outgassing phenomenon*, Advances in Space Research, Vol. 45, p741-749, 2010.

[6] Fest E., *Stray Light Analysis and Control*, SPIE Press, 2013.

[7] Gooding D., Richardson G., Haslehurst A., Smith D., Saunders C., Aglietti G., Blows R., Shore J., Hampson K. and Booth M., *A novel deployable telescope to facilitate a low-cost 1m GSD video rapid-revisit small satellite constellation*, International Conference on Space Optics (Chania Greece), 2018.

[8] Google eart version 7.3.4.8248. (15/03/2015). *Vilamoura 37° 04' 58.61'' N, and 8° 07' 45.08'' W, Eye Alt 3.46km*. Terrametrics [28 march 2022].

[9] Guizar-Sicairos M., Thurman S. T. and Fienup J. R., *Efficient subpixel image registration algorithms*, Optic Letters, Vol. 33(2), p156, 2008.

[10] Heylen J. and Kempenaers M., *Design of a deployable telescope for a CubeSat payload* [Master's Thesis, KULeuven], 2019, Limo. .

[11] Lemaitre G. R., *Astronomical optics an elasticity theory*, Springer-Verlag, 2009.

[12] Liebe C. C., Abramovici A., Bartman R. K., Chapsky, J., Chapsky L., Coste K. and Lam R., *Optical metrology system for radar phase correction on large flexible structure*, IEEE Aerospace Conference Proceedings, p1-7, 2008.

[13] Liebe C. C., Bauman B. W., Clark G. R., Cook R., Kecman B., Madsen K. K., Mao P. and Meras P., Miyasaka H., Cooper M., Scholz C. and Sedaka J., *Design, qualification, calibration and alignment of position sensing detector for the NuSTAR space mission*, IEEE Sensors Journal, Vol. 12(6), p2006-20013, 2012.

[14] Liebe C. C., Burnham J., Cook R., Craig B., Decker T.,Harp I. D., Kecman B., Meras P., Raffanti M., Scholz C., Smith C., Waldman J. and Wu J., *Metrology system for measuring mast motions on the NuSTAR mission*, IEEE Aerospace Conference Proceedings, p1-11, 2010.

[15] Lightsey P. A., Atkinson C. B., Clampin M., Feinberg L., *James Webb Space Telescope: large deployable cryogenic telescope in space*, Optical Engineering, Vol. 51(1), January 2012.

[16] Nakamura Y., Funase R., Nagai M. and Enokuchi A., *Extensible Boom-Based Optical System for Nano-Scale Remote Sensing Satellite ''PRISM''*, 19th Annual AIAA/USU Conference on Small Satellites, 2005.

[17] NASA Ames Research Center, Moffett Field, California, *State of the Art Small Spacecraft Technology*, p24-46, accessed on 05/05/2022, https://www.nasa.gov/sites/default/files/atoms/files/soa2020_final3.pdf.

[18] NuSTAR Science Operations Center, California Institute of Technology (Pasadena CA) and NASA Goddard Spaceflight Center 5Greenbelt, MD), *NuSTAR Observatory Guide*, 2016, accessed on 05/05/2022, https://heasarc.gsfc.nasa.gov/docs/nustar/NuSTAR_observatory_guide-v1.0.pdf.

[19] PiezoMotor and Faulhauber, *Piezo LEGS lineair Series LT20* [CAD models], accessed on 05/04/2022, https://www.faulhaber.com/nl/producten/serie/lt20/.

[20] PiezoMotor, *LT20* [Datascheet], accessed on 06/04/2022, https://piezomotor.com/wp-content/uploads/2019/02/150020-Rev08-LT20-Datasheet.pdf.

[21] Roddier C. and Roddier F., *Wave-front reconstruction from defocused images and the testing of ground-based optical telescopes*, Journal of the Optical Society of America, Vol. 10(11), p2777-2786, 1993.

[22] Schroeder D. J., *Astronomical Optics 2nd edition*, Elsevier Science Publishing, 2000.

[23] Schwartz N., Brzozowski W., Milanova M., Morris K.,Todd, S., Ali Z., Sauvage J.-F., Ward A., Lunney D. and MacLeod D., *High-resolution deployable CubeSat prototype*, Space Telescopes and Instrumentation 2020: Optical, Infrared, and Millimeter Wave, Dec 2020, Online Only, United States. pp.96, 10.1117/12.2562255. hal-03199216.

[24] Segert T., Danziger B., Gork D. and Lieder M., *Dobson space telescope: development of an optical payload of the next generation*, Proc. SPIE 10567, International Conference on Space Optics — ICSO 2006, 105673E (21 November 2017), https://doi.org/10.1117/12.2308063.

[25] Senthil Kumar M., Narayanamurthy C. S., and Kiran Kumar A. S., *Design and analysis of optimum baffle for a Cassegrain telescope*, J. Opt, Vol. 45(2), p180-185, 2016,doi: 10.1007/s12596-015-0296-z.

[26] Verstreken H. and Schreurs S., *Design and analysis of a locking and damping mechanism for a deployable CubeSat telescope structure* [Master's Thesis, KULeuven], 2021, Limo. .

[27] White N. E., Parmar A., and Kunieda H., Nandra K., Ohashi T. and Bookbinder J., *The international X-ray observatory*, AIP Conference Proceedings (arXiv:1001.2843 [astro-ph.IM]), 2010.